Biomaterials Science

Accepted Manuscript

This article can be cited before page numbers have been issued, to do this please use: X. Wang, S. Hu, Y. Fu, W. Xie, G. Li, D. Kong and X. Wang, *Biomater. Sci.*, 2025, DOI: 10.1039/D5BM00879D.

ROYAL SOCIETY OF CHEMISTRY

rsc.li/biomaterials-science

View Article Online
DOI: 10.1039/D5BM00879D

ARTICLE

pH-Responsive Carrier-Free Nanoparticles Based on Teicoplanin and Borneol for Enhanced MRSA Infectious Wound Healing

Received 00th January 20xx,
Accepted 00th January 20xx

DOI: 10.1039/x0xx00000x

Xin Wang[a], Shuyang Hu[a], Ya-nan Fu[a,c], Wensheng Xie[a,*], Guofeng Li[a,*], Dongsheng Kong[b,*], Xing Wang[a,*]

Bacterial infections severely threaten human health, and the drug resistance induced by long-term high-dose antibiotic use is a critical issue, which necessitating new antibacterial strategies. In this study, a pH-responsive carrier-free nanoparticles (BF-TEI NPs) are fabricated based on the Schiff-based bonding between the hydrophilic antibiotic teicoplanin (TEI) and the hydrophobic antibacterial borneol 4-formylbenzoate (BF). Self-assembled BF-TEI NPs enable synchronous release of BF and TEI in infected sites for synergistic antibacterial effects via the acidic microenvironment-triggered Schiff-base bond cleavage. Compared with the physical mixture of BF and TEI, BF-TEI NPs show lower *in vitro* minimum inhibitory and bactericidal concentrations against *Staphylococcus aureus (S. aureus)* and methicillin-resistant *S. aureus* (MRSA), indicating enhanced antibacterial activity. Moreover, BF-TEI NPs effectively eliminate MRSA at the *in vivo* infected sites and accelerate wound healing. Considering the both *in vitro* and *in vivo* good biocompatibility and safety evaluation of BF-TEI NPs. The carrier-free self-assembly strategy of clinical antibiotics offers an innovative approach to overcome drug resistance and improve infectious wound healing.

1. Introduction

Bacterial infections have always been a major challenge threatening global public health and have spread widely in communities and medical institutions.[1–3] Among of them, methicillin-resistant *Staphylococcus aureus* (MRSA), is a Gram-positive bacterium known for causing a wide range of infections, represents a significant public health challenge in the field of pneumonia, endocarditis, sepsis, and wound infections.[4–6] The short or long-term colonization of MRSA may be spontaneously against with the existing treatments.[7,8] Reported prevalence results has demonstrated that about 20% of the population was persistently obstinate nasal carriers and 30% had recurring cases.[9–11] Currently, intensive therapy of invasive MRSA infections mainly dependent on appropriate and combined antibiotic regimens.

Teicoplanin (TEI), as a typical representative of glycopeptide antibiotics, plays a crucial role in the treatment of Gram-positive bacterial infections, especially for MRSA.[12,13] With its unique mechanism of action, TEI can specifically bind to the precursor peptidoglycan of the bacterial cell wall, block the synthesis of the cell wall, and thus inhibit the growth and reproduction of bacteria.[14–16] It is an important "weapon" in the clinical fight against severe resistant bacterial infections. However, the clinical application of TEI currently faces many emergency limitations.[17] On the one hand, long-term use has led to a gradual increase in bacterial resistance due to the mechanisms involving changes in the structure of the cell wall and the activation of efflux pumps, which severely weakens the treatment effect.[18,19] On the other hand, TEI has poor water solubility and limited tissue distribution, making it difficult to reach an effective therapeutic concentration at the infected site. Meanwhile, high-dose use is likely to cause adverse reactions such as nephrotoxicity.[20] How to balance efficacy and safety, overcome resistance, and optimize drug delivery methods to improve the treatment effect have become key scientific problems that need to be solved urgently.[21,22]

In recent decades, with the continuous progress of nanotechnology, various carrier-based drug delivery systems based on the nanoplatform have gradually become an effective means to overcome the defects of clinical applications.[23–26] These carrier-based drug delivery systems can achieve the controlled release of drugs at specific sites, improve the water solubility and bioavailability of drugs.[27,28] Common carriers include liposomes, polymers, metal-organic frameworks, etc.[29–32] However, carrier-based drug delivery systems have the problem of limited drug loading capacity, and the carriers themselves may have side effects on organisms.[33,34] In this context, carrier-free delivery systems that require little or no inert materials have received much attention.[35,36] This system self-assembles to form nanostructures through hydrophobic interactions, electrostatic interactions, or hydrogen bonds between active small molecules, which not only avoids the biosafety hazards

[a] State Key Laboratory of Organic-Inorganic Composites, Beijing Laboratory of Biomedical Materials, College of Life Science and Technology, Beijing University of Chemical Technology, Beijing 100029, China. E-mail: wangxing@mail.buct.edu.cn.
[b] Department of Neurosurgery, First Medical Center of PLA General Hospital, Beijing 100853, China.
[c] School of Nanoscience and Engineering, University of Chinese Academy of Sciences, Beijing 100049, China.
Supplementary Information available: [details of any supplementary information available should be included here]. See DOI: 10.1039/x0xx00000x

View Article Online
DOI: 10.1039/D5BM00837D

brought by nanocarriers but also can achieve a high drug loading rate.[37,38] Previous studies have shown that two molecules without antibacterial activity originally can exhibit extremely strong antibacterial activity after forming superstructures through hydrogen bonds or hydrophobic interactions.[39] However, these nanoparticles have the problem of uncontrollable drug release, which limits their therapeutic effect in practical applications.

In this study, a pH-responsive carrier-free nanoparticles were constructed to overcome the challenge of TEI for MRSA. Specially, the hydrophilic antibiotic TEI and the hydrophobic antibacterial borneol 4-formylbenzoate (BF) are coupled to form carrier-free nanoparticles (BF-TEI NPs) through Schiff-base bonding and self-assembly strategy (**Scheme 1**). Stimulated by the acidic microenvironment at the infected site, BF and TEI are released synchronously via the breaking of Schiff-based bond to exert a synergistic antibacterial effect. It is notably that BF-TEI NPs present good stability in normal tissue conditions, which helps to prolong their circulation time in blood and long-term antibacterial effects. Both *in vitro* and *in vivo* results show that BF-TEI NPs have a more significant antibacterial effect and enhanced infectious wound healing when comparing with the physical combined administration of BF and TEI. Considering the excellent biosafety, this carrier-free delivery strategy provides safe, simple, and efficient approach for the treatment of bacterial infections.

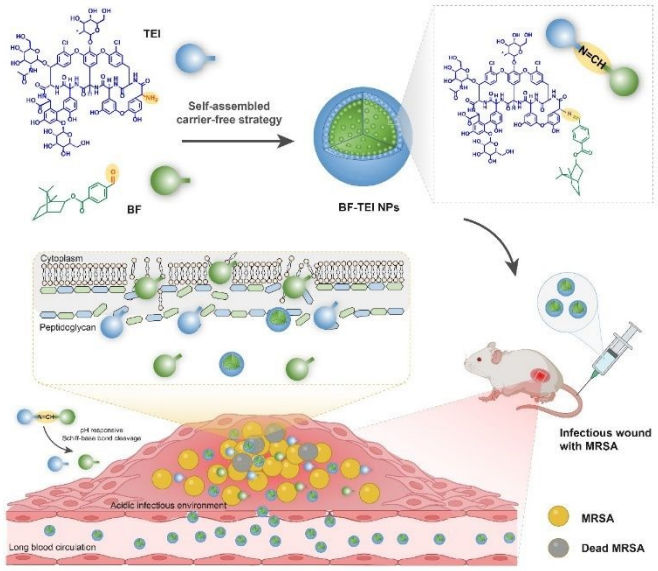

Scheme 1. The preparation of self-assembled carrier-free BF-TEI NPs for enhanced MRSA infectious wound healing.

2. Experimental methods

2.1 Materials

Teicoplanin (TEI) (≥98%), Nile red (NR, ≥98%), Cy7.5 (≥97%), and dimethyl sulfoxide (DMSO) were all purchased from J&K Scientific (China). Tryptone soybean broth (TSB) and tryptone soybean agar (TSA) were purchased from Sinopharm Chemical Reagent Co., Ltd. (China). The AO/PI double staining kit and BCA protein detection kit were purchased from Solarbio Science & Technology Co., Ltd. (China). Borneol 4-formylbenzoate (BF) was self-prepared in the laboratory. The *Staphylococcus aureus* (*S. aureus*) used had the accession number ATCC25923 and was preserved by the China Center of Industrial Culture Collection. The methicillin-resistant *S. aureus* used had the accession number S1857 and was clinically isolated from the Affiliated Hospital of the Chinese Academy of Military Medical Sciences. Male Balb/c mice (6 weeks old) were purchased from Beijing Charles River Laboratory Animal Co., Ltd. (China). All animals were treated and cared for in accordance with the Guide for the Care and Use of Laboratory Animals of the National Research Council of the United States and were supervised and evaluated by the SPF Animal Department of the Clinical Research Institute of China-Japan Friendship Hospital (No. zryhyy 12-20-08-3).

2.2 Preparation of BF-TEI NPs

TEI (120 mg) and BF (5 mg) were dissolved in 3 mL of DMSO and reacted at 1500 rpm and 37°C for 6 h. Subsequently, 12 mL of deionized water was slowly and uniformly added dropwise to the mixture, and the reaction was continued for another 3 h. Finally, the solution was placed into a dialysis bag (3500 Da), dialyzed against deionized water for 48 h, and lyophilized to obtain BF-TEI NPs.

2.3 Characterization of BF-TEI NPs

The structures of BF, TEI, and BF-TEI NPs were characterized using a ^{1}H nuclear magnetic resonance (NMR) spectrometer (400 MHz, Bruker, Germany). The morphological features of BF-TEI NPs were observed via scanning electron microscopy (SEM, JSM-7800F, JEOL, Japan) and transmission electron microscopy (TEM, S-4700, Hitachi, Japan). The particle size distribution and zeta potential of BF-TEI NPs in deionized water were evaluated using a dynamic light scattering (DLS) analyzer (Zetasizer Nano ZS, Malvern Panalytical, UK). The stability of BF-TEI NPs was investigated by continuously monitoring these parameters over 7 days.

2.4 pH-responsive performances of BF-TEI NPs

BF-TEI NPs were dissolved in buffer solutions with varying pH values (pH = 3, 5.5, 7.4) and loaded into dialysis bags (3500 Da). The dialysis bags were then placed in centrifuge tubes containing the corresponding pH buffer solutions and incubated at 37°C with shaking at 3000 rpm to facilitate complete cleavage. At predefined time intervals, aliquots of the dialysate were collected, and an equal volume of fresh PBS buffer was replenished. The absorbance at 279 nm was measured using a UV-Vis spectrophotometer (UV-2600, Shimadzu, Japan) to determine the drug content at each time point, and release profiles were plotted accordingly. Concurrently, the hydrodynamic diameter of BF-TEI NPs under different pH conditions was monitored using DLS to investigate their acid-responsive properties based on particle size changes.

2.5 Antibacterial Activity against *S. aureus* and MRSA

S. aureus and MRSA were selected as model pathogenic bacteria for *in vitro* antibacterial evaluation. Four experimental groups were established: (1) treatment with TEI alone, (2) treatment with BF alone, (3) physical mixture of TEI and BF (MIX), and (4) treatment

with BF-TEI NPs (NPs). The TEI/BF group was prepared to maintain the stoichiometric equivalence to BF-TEI NPs. Specifically, continuous dilutions of each treatment group were prepared. 100 μL of the dilution was co-incubated with 100 μL of the bacterial suspension (1×10^6 CFU/mL) in a 96-well plate and cultured at 37°C for 24 h. The absorbance at 600 nm was detected by a microplate reader to evaluate the minimum inhibitory concentration (MIC) of BF-TEI NPs. Then, 100 μL of the bacterial suspension after MIC culture was spread on the agar medium and cultured overnight at 37°C to determine the minimum bactericidal concentration (MBC) of BF-TEI NPs.

2.6 Synergistic bactericidal performance of BF and TEI

MRSA was selected as the model pathogenic bacteria for synergistic antibacterial evaluation. The drug concentrations were set according to the MIC results. Different concentrations of the BF/TEI mixture were prepared and co-incubated with 100 μL of the bacterial suspension (1×10^6 CFU/mL) in a 96-well plate at 37°C for 24 h. The absorbance at 600 nm was detected by a microplate reader. The fractional inhibitory concentration (FIC) was calculated according to Formula 1 to evaluate the synergistic effect of BF and TEI.

FIC index = (MIC of BF in combination / MIC of BF) + (MIC of TEI in combination / MIC of TEI) ……(Formula 1)

2.7 Live/Dead Staining

1 mL of the drug solution (BF 6 μg/mL, TEI 14 μg/mL, BF/TEI (MIX) 6/14 μg/mL, BF-TEI NPs 20 μg/mL) was co-incubated with 300 μL of the MRSA suspension (1×10^9 CFU/mL) at 37°C for 0 h and 24 h. Then, it was measured using a Live/Dead Bacterial Viability Kit (AO/PI, brand, country) according to the kit instructions. A confocal laser scanning microscope (CLSM, model, brand, country) was used to obtain images, and Image J software (v1.8.0) was used for quantitative analysis.

2.8 Evaluation of Bacterial Membrane Damage

1 mL of the drug solution was co-incubated with 300 μL of the MRSA bacterial suspension (1×10^9 CFU/mL) at 37°C for 24 h. The bacterial pellet was obtained by centrifugation at 7500 rpm for 3 min. The pellet of each group was fixed with 1 mL of glutaraldehyde fixing solution at 4°C for 2 h, and then dehydrated stepwise with 50%, 70%, 90%, and 100% ethanol. Finally, the morphological changes of bacteria were observed by SEM.

2.9 Protein Leakage Measurement

1 mL of the drug solution was co-incubated with 300 μL of the MRSA bacterial suspension (1×10^9 CFU/mL) at 37°C for 24 h. The supernatant was obtained by centrifugation at 7500 rpm for 3 min. Then, 20 μL of the supernatant of each group was co-incubated with 200 μL of the BCA working solution at 37°C for 30 min, and the absorbance at 562 nm was detected by a microplate reader. The corresponding protein concentration was calculated according to the bovine serum albumin (BSA) standard curve, and then the relative leakage rate was calculated according to Formula 2.

Relative leakage rate (%) = ((Sample concentration - Blank concentration) / (RIPA concentration - Blank concentration)) × 100% ……(Formula 2)

2.10 Co-localization of Bacteria and BF-TEI NPs

Firstly, BF-TEI NPs were stained with the green fluorescent dye coumarin-6 ($\lambda_{ex}/\lambda_{em}$ = 270/310 nm) (Cou-6@NPs), and MRSA was stained with Nile Red (NR, $\lambda_{ex}/\lambda_{em}$ = 515/570 nm) (NR@MRSA). Then, 1 mL of the Cou-6@NPs solution was co-incubated with 300 μL of the NR@MRSA suspension at 37°C for 3 h. The pellet was obtained by centrifugation at 7500 rpm for 3 min. The pellet was washed twice with normal saline and resuspended in 100 μL of normal saline, and the results were detected by CLSM.

2.11 *In Vivo* Biodistribution Measurement

200 μL of the MRSA bacterial suspension (1×10^8 CFU/mL) was injected subcutaneously into the back of mice to establish an infection model. BF-TEI NPs were labelled with the fluorescent Cy7.5 (λex/λem = 745/820 nm) (Cy7.5@NPs). Mice were intravenously injected with Cy7.5@NPs, and in vivo imaging was performed using an *in vivo* optical imaging system (IVIS) at predetermined time points (1, 3, 6, 9, 12, 24, 36, 48 h). The *in vivo* fluorescent images and the relative fluorescence intensity values at the wound infection site were recorded. After 48 h, the mice were euthanized, and the main organs (skin, heart, liver, spleen, lung, kidney) were collected, and the fluorescent images and relative fluorescence intensity values of each organ were recorded by IVIS.

2.12 *In Vivo* therapeutic efficacy

200 μL of the MRSA bacterial suspension (1×10^8 CFU/mL) was injected subcutaneously into the back of mice to establish an infection model. The mice were randomly divided into three groups (PBS group, MIX group, BF-TEI NPs group). 200 μL of the solution was administered via tail vein injection every other day for a treatment cycle of 10 days. Meanwhile, the body weight of the mice and the wound area were recorded daily. After the treatment, the mice were euthanized, and the skin at the infected site was collected for tissue grinding and H&E staining.

2.13 *In vitro* and *in vivo* Biocompatibility Evaluation

100 μL of L929 cells (1×10^4 cells/well) were seeded in a 96-well plate and co-incubated with 100 μL of solutions of different concentrations (128 μg/mL, 64 μg/mL, 32 μg/mL, 16 μg/mL, 8 μg/mL, 4 μg/mL, 2 μg/mL, 1 μg/mL) of BF, TEI, MIX, and BF-TEI NPs for 24 h. Then, 10 μL of MTT solution was added and incubated for an additional 4 h. The crystalline substances were fully dissolved with SDS solution in the dark, and the absorbance was measured at 570 nm. 0.2 mL of the erythrocyte suspension was incubated with 0.8 mL of BF-TEI NPs solutions of different concentrations (128 μg/mL, 64 μg/mL, 32 μg/mL, 16 μg/mL, 8 μg/mL, 4 μg/mL) at 37°C for 3 h. After the incubation, 100 μL of the supernatant was taken, and the absorbance was measured at 540 nm.

For *in vivo* biosafety evaluation, healthy mice were randomly divided into three groups (PBS group, MIX group, BF-TEI NPs group). 200 μL

of the solution was administered via tail vein injection every other day for a treatment cycle of 10 days. After the treatment, blood was collected from the eyeball for blood biochemical analysis, and the main organs (heart, liver, spleen, lung, kidney) were collected for H&E staining.

2.14 Statistical analysis

All data were presented as mean values ± SD, and the statistical difference was calculated by two-tailed student's t test and one-way ANOVA. *p < 0.05, **p < 0.01, ***p < 0.001, and ****p < 0.0001.

3. Results and discussion

3.1 Preparation and Characterization of BF-TEI NPs

The carrier-free BF-TEI NPs were prepared via Schiff-base bonding reaction and self-assembly strategy (**Fig. 1A**). Particularly, BF was synthesized via esterification reaction between 2-borneol and 4-formylbenzoic acid (**Fig. S1**). The fine molecular structure was confirmed by proton nuclear magnetic resonance (^{1}H NMR) analysis (**Fig. S2**). Then, to synthesize binary BF-TEI molecule, TEI and BF were completely dissolved and mixed in DMSO for coupling via Schiff- base bonding reaction under high-speed stirring. ^{1}H NMR spectrum of binary BF-TEI molecule showed the typical Schiff-base bonding (δ 8.413 ppm), indicating the successful reaction (**Fig. S3**). Subsequently, BF-TEI self-assembled in an aqueous environment to form nanoscale carrier-free BF-TEI NPs in hydrophilic-hydrophobic interfaces (**Fig. 1A**). The suspension of BF-TEI NPs in deionized water presented a uniform and stable emulsion state and exhibited a significant Tyndall effect (**Fig. 1B**), intuitively demonstrating the successful construction of the nanoscale structure. The microscopic morphology and structure of BF-TEI NPs was observed by scanning electron microscopy (SEM) and transmission electron microscopy (TEM). The results showed that the nanoparticles had a regular and smooth spherical structure, with a uniform particle size distribution and a solid internal morphology (**Fig. 1C&D**). Dynamic light scattering (DLS) analysis indicated that the average particle size of BF-TEI NPs was concentrated between 200-300 nm with a narrow polydispersity index (PDI) of 0.266 (**Fig. 1E**), indicating the good dispersibility. Further Zeta potential analysis showed that the surface charge of BF-TEI NPs was about -20 mV (**Fig. 1F**), which was mainly attributed to the abundant hydroxyl (-OH) and carboxyl (-COOH) groups on the particle surface.[40] Through further stability monitoring for 7 consecutive days, it was found that the Zeta potential of BF-TEI NPs stably remained between -18 mV and -22 mV, and the particle size fluctuated in the range of 180-210 nm (**Fig. 1G**), confirming the excellent stability in aqueous environment.

Based on ^{1}H NMR spectral analysis, the aldehyde group signal peak of BF-TEI NPs at δ 10.12 ppm completely disappeared, and a new characteristic signal peak of the imine bond appeared at δ 8.413 ppm (**Fig. 1H**) when comparing with the raw BF, clearly demonstrating the successful formation of Schiff-base bonds. It is calculated that the drug loading efficiency (DLE) of TEI and BF was 71.61% and 28.39%, respectively (**Table S1**), demonstrating that there was few free TEI loaded in NF-TEI NPs. The kinetic curve of drug release behaviour showed that the drug release amount of BF-TEI NPs within 48 h was only about 20%, reflecting a stable self-assembled structure under physiological pH 7.4 conditions. However, under acidic conditions (pH 5.5) that simulating the microenvironment of infection, the cumulative release amount of TEI within 48 h could be increased to approximately 60% (**Fig. 1I**). Combined with DLS tests, it was found that as the pH value decreased, the hydrodynamic diameter of BF-TEI NPs changed significantly (**Fig. 1J**). This phenomenon was attributed to the acid sensitivity of the Schiff-base bonds, and their cleavage in an acidic environment promoted the disintegration of the nanoparticle structure and accelerated drug release.[41–43] The above results fully demonstrate that BF-TEI NPs possess the characteristic of pH-responsive drug release performance and can precisely respond to the acidic microenvironment of infected tissues to achieve controlled drug release.

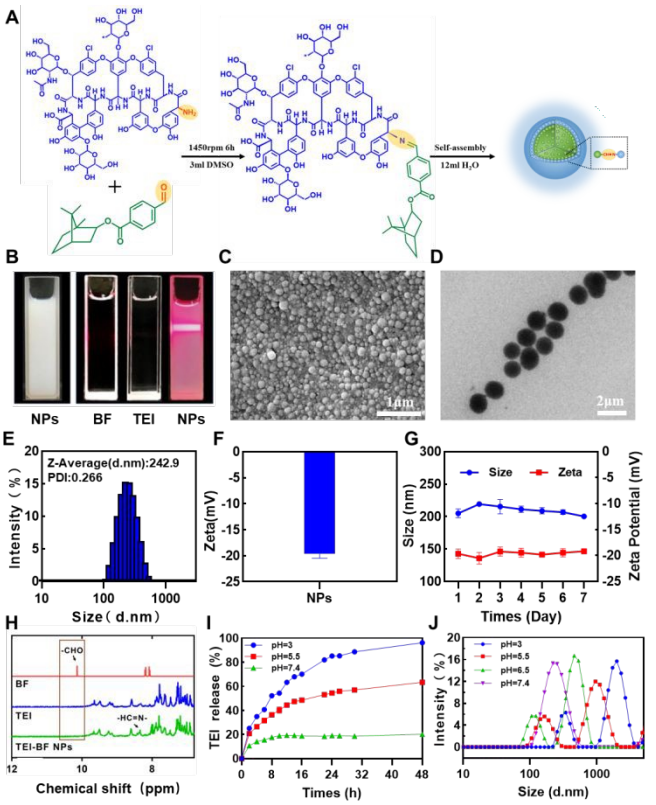

Fig. 1. Preparation and basic characterization of BF-TEI NPs. (A) Schematical illustration of the preparation process of BF-TEI NPs; (B) Presentation of the appearance and physical properties of BF-TEI NPs; (C) SEM images of BF-TEI NPs; (D) TEM images of BF-TEI NPs; (E) Particle size distribution of BF-TEI NPs; (F) Zeta potential of BF-TEI NPs; (G) Results of the stability test of BF-TEI NPs; (H) ^{1}H NMR spectrum of BF-TEI NPs; (I) Cumulative release curve of TEI within 0 to 48 h under different pH buffers; (J) Changes in the particle size of BF-TEI NPs under different pH buffers.

3.2 In Vitro Antibacterial Activity of BF-TEI NPs

View Article Online
DOI: 10.1039/D5BM00878D

To systematically evaluate the antibacterial efficacy of BF-TEI NPs, *S. aureus* and MRSA were chosen as *in vitro* model strains to determine their MIC and MBC. As shown in Table 1, the MIC values of free BF, free TEI, physical mixture of BF and TEI (MIX), and BF-TEI NPs to *S. aureus* were 8 μg/mL, 0.5 μg/mL, 1.25 μg/mL, and 0.63 μg/mL, respectively **(Fig. S4**). Compared with the MIX group, the MIC of BF-TEI NPs decreased by about 50%, demonstrating the efficiency of self-assembled carrier-free strategy. In the determination of MBC, the corresponding values were 32 μg/mL, 16 μg/mL, 20 μg/mL, and 5 μg/mL, respectively. The bactericidal activity of BF-TEI NPs was significantly increased and presented a 4 time-fold better than that of the MIX group. These results indicate that BF-TEI NPs can effectively reduce the dosage of free TEI by optimizing the form of nanoparticles, thereby reducing the potential risk of adverse reactions caused by high-dose medication.

In addition, the bactericidal efficacy of BF-TEI NPs to MRSA was systematically examined. As shown in Table 1, the MIC values of BF, TEI, MIX, and BF-TEI NPs against MRSA were 16 μg/mL, 4 μg/mL, 10 μg/mL, and 5 μg/mL, respectively (**Fig. S5**). The MIC value of BF-TEI NPs was 50% lower than that of the MIX group, which is in agreement with the results of *S. aureus*. Meanwhile, the results of MBC determination showed that the corresponding values were > 64 μg/mL, 32 μg/mL, 20 μg/mL, and 10 μg/mL (**Fig. S6**). Luckily, the bactericidal activity of BF-TEI NPs was increased by 2 times compared with the MIX group. This excellent performance can be attributed to the unique spherical nanostructure of BF-TEI NPs and its large specific surface area, which not only significantly increases the contact area with bacteria but also facilitates its penetration of the bacterial cell wall, thus achieving efficient antibacterial effects.[44–46]

Table 1 Evaluation of *in vitro* antibacterial performance against *S. aureus* and MRSA

		BF (μg/mL)	TEI (μg/mL)	MIX (μg/mL)	BF-TEI NPs (μg/mL)
S. aureus	MIC	8	0.5	1.25	0.63
	MBC	32	16	20	5
MRSA	MIC	16	4	10	5
	MBC	>64	32	20	10

3.3 Antimicrobial Mechanism of BF-TEI NPs

The antibacterial mechanism and targeting properties of BF-TEI NPs were systematically investigated to reveal the advantages of self-assembled carrier-free nanoparticles compared to free antibiotics. Firstly, the fractional inhibitory concentration (FIC) index was used to evaluate the synergistic antibacterial effect of BF and TEI.[47] As shown in **Fig. 2A**, when the concentration of BF and TEI was 2 μg/mL and 0.125 μg/mL, respectively, the calculated FIC value was 0.5. According to the FIC evaluation criteria (FIC ≤ 0.5 indicates synergy; 0.5 < FIC ≤ 1 indicates an additive effect; 1 < FIC ≤ 2 indicates no interaction; FIC > 2 indicates antagonism), [48,49] a synergistic antibacterial effect between BF and TEI was clearly confirmed. Previous studies have shown that as a glycopeptide antibiotic, TEI exhibits strong lipophilicity due to its unique fatty chain structure, allowing it to efficiently penetrate tissues and cells, interfere with the normal synthesis of cell walls and membranes, and ultimately cause the death of Gram-positive bacteria.[50] BF, as a penetration enhancer, can effectively loosen the bacterial cell wall and increase membrane permeability, helping drugs penetrate physiological barriers to reach target sites.[51] Therefore, the synergistic effect of the two endows BF-TEI NPs with more excellent antibacterial performance.

The antibacterial effect of BF-TEI NPs was further analysed through live/dead staining measurement, SEM observation, and quantitative analysis of protein leakage. The live/dead staining results (**Fig. 2B**) showed that green fluorescence (representing viable bacteria) dominated in the bacterial populations treated with free BF or TEI alone, indicating that bacterial activity was not severely inhibited. However, after treatment with MIX and BF-TEI NPs, red fluorescence (representing damaged or dead bacteria) increased significantly (**Fig. 2C**). Quantitative analysis of fluorescence intensity further confirmed that the bactericidal effect of BF-TEI NPs was particularly prominent, which was highly consistent with the MIC and MBC results. SEM images of bacterial (**Fig. 2D**) directly presented the morphological changes of bacteria. It presented that untreated bacterium had smooth surfaces and intact membrane structures, while local depressions appeared on the bacterial cell membrane after treatment with BF and TEI. In contrast, MIX treatment caused obvious membrane shrinkage, and the BF-TEI NPs treatment group showed significant membrane damage, surface cracks, and collapse. Furthermore, the quantitative protein leakage analysis (**Fig. 2E**) exhibited the amount of bacterial protein leakage after BF-TEI NPs treatment increased significantly, and it was significantly higher than that of the MIX treatment group at an equivalent dose, directly indicating that the nanostructure of BF-TEI NPs significantly enhanced the ability to damage the bacterial cell membrane via bacterial targeting.

To verify the bacterial targeting ability of BF-TEI NPs, a co-localization experiment was carried out using coumarin-6 labelled BF-TEI NPs (Cou-6@NPs) and Nile Red labelled MRSA (NR@MRSA). As shown in **Fig. 2F**, after co-incubation of Cou-6@NPs and NR@MRSA, the overlapping area showed yellow fluorescence, visually demonstrating their co-localization. Further extraction and analysis of the fluorescence signals (**Fig. 2G**) revealed that the fluorescence trajectories of the two groups highly overlapped and the fluorescence intensities were basically the same, it is notably that BF-

TEI NPs have good bacterial targeting recognition and enrichment abilities.

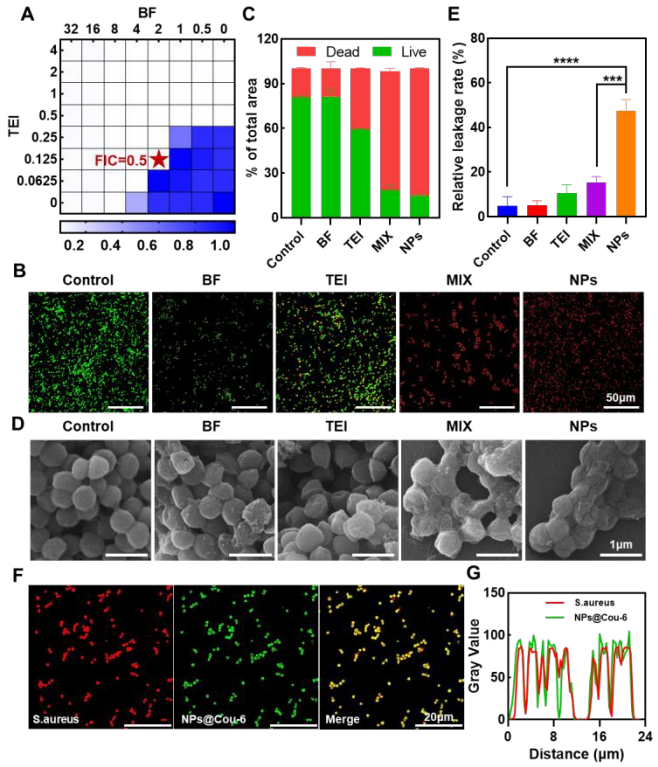

Fig. 2. Study on the *in vitro* antibacterial mechanism: (A) Evaluation of the synergistic effect of the combined antibacterial action of BF and TEI; (B) Live/dead staining images of MRSA after different sample treatments for 24 h; (C) Quantitative analysis of the live/dead staining; (D) SEM images of the effect of different sample treatments on MRSA; (E) Protein leakage situation of MRSA treated with different samples; (F) Confocal images of NR@MRSA co-incubated with Cou-6@NPs for 3 h; (G) Fluorescence co-localization curve of NR@MRSA and Cou-6@NPs.

3.4 *In Vivo* Biodistribution Evaluation

To deeply explore the biodistribution characteristics of BF-TEI NPs in mice, the IVIS *in vivo* imaging system was used to conduct real-time tracking of Cy7.5-labelled BF-TEI NPs (Cy7.5@NPs). As shown in the experimental model of **Fig. 3A**, 1 h post intravenous injection, the fluorescence signal of Cy7.5@NPs could be clearly detected at the infected site and in major organs (**Fig. 3B**). With the time goes by, the fluorescence intensity at the infected site gradually increased, while the fluorescence intensities of the liver and lungs gradually decreased. The quantitative analysis data showed that the fluorescence intensity at the infected site reached its peak at 9 h (**Fig. 3C**). After 48 h of administration, the main organs of the mice (including the skin, heart, liver, spleen, lung, and kidney) were detected ex vivo. The results showed that Cy7.5@NPs were mainly distributed in the liver, followed by the kidney. The average fluorescence intensity (MFI) at the infected site was twice more than that of the uninfected site (**Fig. 3D&E**). Previous studies have shown that nanoparticles have a longer residence time in the blood compared with free small molecule drugs,[20] which is consistent with the results of *in vivo* biodistribution. These results strongly demonstrate that BF-TEI NPs have a long residence time *in vivo* and can effectively accumulate at the infected site, providing favorable conditions for the exertion of their antibacterial activity.

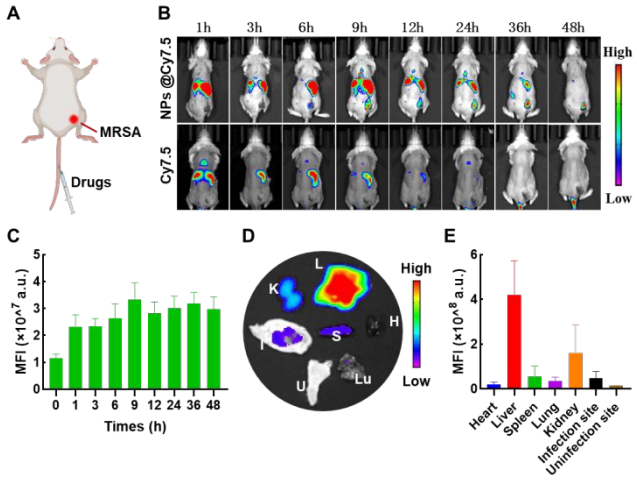

Fig. 3. *In vivo* distribution characteristics and targeting enrichment ability of BF-TEI NPs. (A) Schematic diagram of the construction of the mouse infection model and the administration method; (B) Imaging results of the *in vivo* fluorescence distribution after intravenous injection of Cy7.5@NPs and free Cy7.5 in mice; (C) Dynamic changes in the fluorescence intensity at the subcutaneous abscess site of mice at different time points; (D) Ex vivo fluorescence imaging of the main organs and infected skin tissues of mice 48 h after intravenous injection; (E) Results of the quantitative analysis of the mean MFI of various organs and skin tissues of mice.

3.5 *In Vivo* Therapeutic Efficacy on Subcutaneous Abscesses Model

Previous results inspire us to assess the *in vivo* therapeutic efficacy of BF-TEI NPs. Therefore, a subcutaneous abscess mouse model was constructed to systematically evaluate the *in vivo* antibacterial efficacy and wound healing efficiency of BF-TEI NPs. As shown in **Fig. 4A**, extensive ulcer symptoms appeared on the wound surface at the initial stage of infection, indicating the successful establishment of the infection model. As the treatment progressed, the wounds in each experimental group showed different degrees of healing. It is clear that the wound healing rate of the BF-TEI NPs group was significantly better than that of the other groups (BF, TEI, and MIX), and there was almost no obvious scab residue on the wound surface after the 10 days' treatment (**Fig. 4B**). Meanwhile, the simulation analysis of the wound healing process and the wound area change curve (**Fig. 4C&D**) obviously presented the significant advantage of BF-TEI NPs in accelerating wound healing. Besides, the body weight of the mice in the BF-TEI NPs group increased more significantly during the treatment period (**Fig. 4E**), reflecting the improvement of the overall health status of the mice in this group.

To further show the bacteria-eliminating ability, the colony counting of remained MRSA was made and the results showed that a large number of bacteria remained in the infected site of the PBS group. However, both the MIX group and the BF-TEI NPs group showed significant bacteria-clearing effects, and the BF-TEI NPs group was particularly prominent (**Fig. 4F**). Quantitative analysis showed that the number of colony-forming units (CFU) in the BF-TEI NPs group was significantly lower than that in the MIX group **(Fig. 4G**), confirming its highly effective inhibitory effect on *in vivo* bacterial infection. Finally, a deep analysis of tissue repair was carried out by haematoxylin-eosin (H&E) staining. The images showed that there were obvious defects in the dermal tissue of the mice in the PBS group. Although the MIX group achieved basic repair of the dermal tissue, epidermal thickening occurred. For BF-TEI NPs group , not only the dermal structure restored to integrity, but also the regeneration of hair follicles and other skin appendage structures was observed (**Fig. 4H**).[52,53], demonstrating the best tissue repair efficacy. Taken together, BF-TEI NPs can not only effectively eliminate bacterial infection *in vivo,* but also significantly promote the rapid healing of infected wounds.

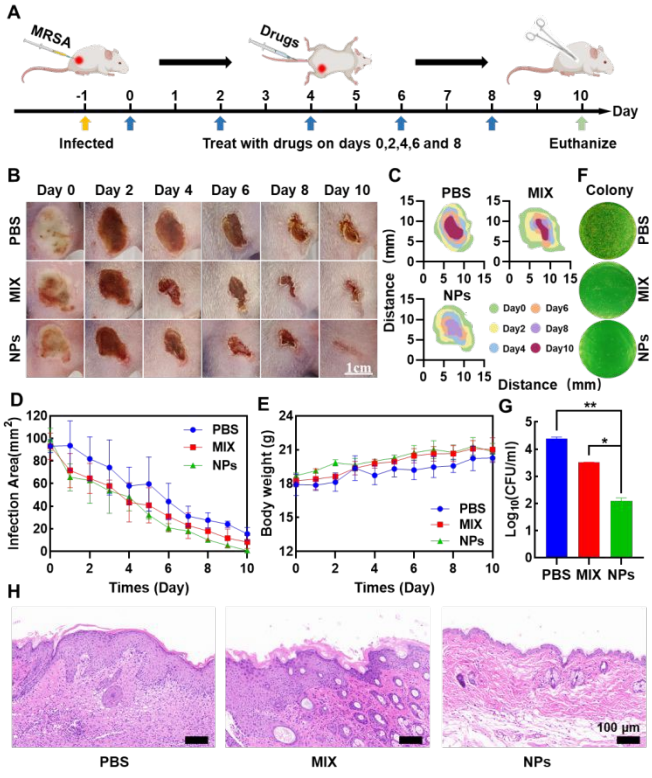

Fig. 4. *In vivo* treatment effect of the mouse model of subcutaneous abscess. (A) Schematic diagram of the construction process of the subcutaneous abscess model and the treatment intervention. (B) Dynamic observation of the healing of the infected wound surface under different treatment groups. (C) Visual simulation diagram of the healing process of the infected skin wound of mice in each group. (D) Dynamic change curve of the wound area over the treatment time. (E) Trend curve of the body weight change of mice during the treatment period. (F) Imaging results of the colony culture coating at the infected site at the end of the treatment. (G) Quantitative analysis of the CFU of the infected tissue after the treatment. (H) Observation of the pathological sections stained with H&E of the infected tissue after the treatment.

3.6 Biosafety Evaluation

Finally, a systematic evaluation at the cellular level, blood compatibility level, and the whole animal level were conducted to comprehensively evaluate the biosafety of BF-TEI NPs. The results of the cytotoxicity experiment (**Fig. 5A**) showed that when the co-incubation concentration reached approximately 128 μg/mL, the BF and MIX groups exhibited significant cytotoxicity to L929 cells, while the cell viability of the BF-TEI NPs group remained above 70%, demonstrating that BF-TEI NPs can maintain good cell safety even at high concentrations. Furthermore, the haemolysis experiment further confirmed the blood compatibility of BF-TEI NPs. When the concentration was as high as 64 μg/mL, the haemolysis rate was still lower than 5% (**Fig. 5B**), meeting the safety requirements of biomaterials in contact with blood.

At the whole animal level, healthy mice were administered PBS, MIX, and BF-TEI NPs via tail vein injection, followed by blood biochemical analysis (**Fig. 5C**). The results showed that compared with the PBS group, there were no statistical differences in various biochemical indicators (ALT, ALB, AST, UA, CREA, and UREA) in the BF-TEI NPs group. This clearly indicates that BF-TEI NPs do not have adverse effects on the liver and kidney functions of mice at the set drug dose. Furthermore, H&E staining was performed on the main organs (heart, liver, spleen, lung, kidney) of mice (**Fig. 5D**), and no obvious histological, morphological, and pathological abnormalities were found in all treatment groups.[54] Combining the above results, BF-TEI NPs exhibit good biosafety both *in vitro* and *in vivo*, providing a solid safety guarantee for their further clinical applications.

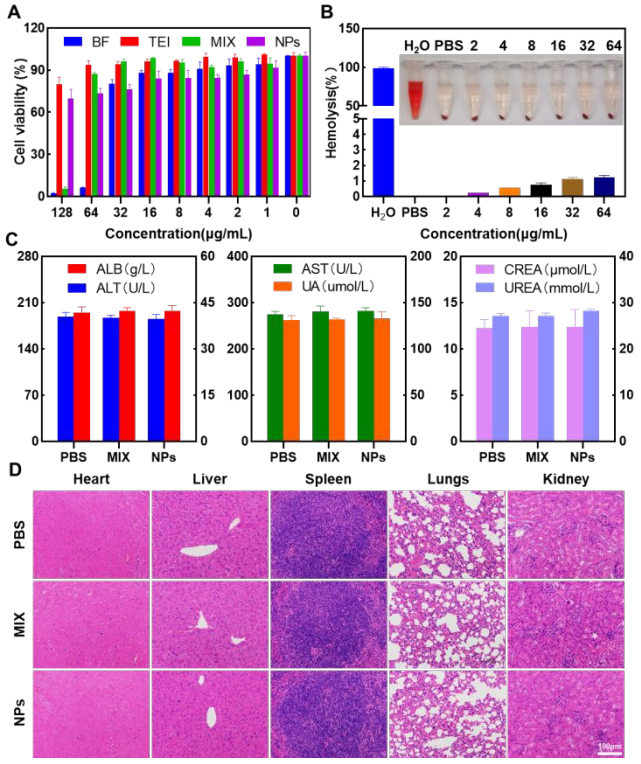

Fig. 5. Biosafety Assessment. (A) The relative viability of L929 cells after being treated with different concentrations of BF-TEI NPs for 24 h; (B) The hemolytic effect of different concentrations of BF-TEI NPs on red blood cells; (C) The results of blood biochemical analysis conducted on healthy mice (ALT, ALB, AST, UA, CREA, and UREA); (D) H&E staining images of the main organs (including the heart, liver, spleen, lungs and kidneys) of healthy mice after different treatments.

4. Conclusion

In conclusion, this study successfully constructed carrier-free BF-TEI NPs with pH-responsive properties based on Schiff-base reaction and self-assembly strategy. Self-assembled BF-TEI NPs enable synchronous release of BF and TEI in infected sites for synergistic antibacterial effects via the acidic microenvironment-triggered Schiff-base bond cleavage. Compared with the physical mixture of BF and TEI, BF-TEI NPs show lower *in vitro* minimum inhibitory and bactericidal concentrations against *S. aureus* and MRSA, indicating enhanced antibacterial activity. The antibacterial mechanism mainly involves enhancing bacterial target of nanostructure, causing damage of cell membrane, and inducing protein leakage. Meanwhile, BF-TEI NPs possess a better retention effect *in vivo*, and continuously exert antibacterial effects and also effectively promoting the rapid healing of infected wounds. Considering the excellent biosafety, the self-assembled carrier-free strategy based on two antibiotics proposed in this study has opened up a new path to overcome the limitation of free single antibiotics for the treatment of MRSA infections.

Author contributions

Xin Wang: Conceptualization, Methodology, Writing-review & editing. Shuyang Hu: Methodology, Data analysis. Yanan Fu: Methodology, Data analysis. Wensheng Xie: Methodology, Funding acquisition, Writing-review & editing. Guofeng Li: Methodology, Funding acquisition, Writing-review & editing. Dongsheng Kong: Conceptualization, Writing-review & editing. Xing Wang: Conceptualization, Funding acquisition, Writing-review & editing.

Conflicts of interest

There are no conflicts to declare.

Data availability

The data supporting this article have been included as part of the Supplementary Information.

Acknowledgements

This research was supported by the National Natural Science Foundation of China (52273118, 22275013), the Natural Science Foundation of Beijing Municipality (2254093), the project of Science and Technology of Yinchuan (2024SFZD004). Many thanks for the funding support by union project of BUCT-CJFH biomedical center (XK2023-16, PT2407, 2024-NHLHCRF-YXHZ-MS-05), union project of BUCT-PUTH (PT2517), and Fundamental Research Funds for the Central Universities (PY2508, QNTD2023–01, buctrc202419).

References

1 K. S. Ikuta, C. Zhong, M. Zoladl, A. Zumla, S. I. Hay, C. Dolecek, B. Sartorius, C. J. L. Murray and M. Naghavi, *The Lancet*, 2022, **400**, 2221–2248.
2 K. Xiao, Y. Cao, Z. Han, Y. Zhang, L. D. W. Luu, L. Chen, P. Yan, W. Chen, J. Wang, Y. Liang, X. Shi, X. Wang, F. Wang, Y. Hu, Z. Wen, Y. Chen, Y. Yang, H. Yu, L. Xie and Y. Wang, *Sig Transduct Target Ther*, 2025, **10**, 5.
3 W. Feng, M. Chittò, W. Xie, Q. Ren, F. Liu, X. Kang, D. Zhao, G. Li, T. F. Moriarty and X. Wang, *ACS Nano*, 2024, **18**, 8017–8028.
4 J. Jia, M. Zheng, C. Zhang, B. Li, C. Lu, Y. Bai, Q. Tong, X. Hang, Y. Ge, L. Zeng, M. Zhao, F. Song, H. Zhang, L. Zhang, K. Hong and H. Bi, *Sci. Adv.*, 2023, **9**, eadg5995.
5 P. L. Wantuch and D. A. Rosen, *Trends in Immunology*, 2023, **44**, 826–844.
6 C. Cilloniz, C. Dominedò, A. Gabarrús, C. Garcia-Vidal, J. Becerril, D. Tovar, E. Moreno, Juan. M. Pericás, C. R. Vargas and A. Torres, *Journal of Infection*, 2021, **82**, 76–83.
7 X. Kang, X. Yang, F. Bu, W. Feng, F. Liu, W. Xie, G. Li and X. Wang, *ACS Appl. Mater. Interfaces*, 2024, **16**, 3202–3214.
8 D. Hu, L. Zou, B. Li, M. Hu, W. Ye and J. Ji, *ACS Biomater. Sci. Eng.*, 2019, **5**, 5169–5179.
9 S. Singh, A. Numan, H. H. Somaily, B. Gorain, S. Ranjan, K. Rilla, H. R. Siddique and P. Kesharwani, *Materials Science and Engineering: C*, 2021, **129**, 112384.
10 J. Davis, S. Hal and S. Tong, *Semin. Respir. Crit. Care Med.*, 2015, **36**, 3–16.

11 D. Liu, Y. Xi, S. Yu, K. Yang, F. Zhang, Y. Yang, T. Wang, S. He, Y. Zhu, Z. Fan and J. Du, *Biomaterials*, 2023, **293**, 121957.
12 D. M. Campoli-Richards, R. N. Brogden and D. Faulds, *Drugs*, 1990, **40**, 449–486.
13 I. Odenholt, E. Löwdin and O. Cars, *Clinical Microbiology and Infection*, 2003, **9**, 930–937.
14 S.-Y. Lyu, Y.-C. Liu, C.-Y. Chang, C.-J. Huang, Y.-H. Chiu, C.-M. Huang, N.-S. Hsu, K.-H. Lin, C.-J. Wu, M.-D. Tsai and T.-L. Li, *J. Am. Chem. Soc.*, 2014, **136**, 10989–10995.
15 J.-G. Lee, C. Sagui and C. Roland, *J. Am. Chem. Soc.*, 2004, **126**, 8384–8385.
16 D. L. Boger, *Medicinal Research Reviews*, 2001, **21**, 356–381.
17 A. P. Johnson, A. H. Uttley, N. Woodford and R. C. George, *Clin Microbiol Rev*, 1990, **3**, 280–291.
18 T. J. Foster, *FEMS Microbiology Reviews*, 2017, **41**, 430–449.
19 A. M. Sefton, *Drugs*, 2002, **62**, 557–566.
20 P. Huang, D. Wang, Y. Su, W. Huang, Y. Zhou, D. Cui, X. Zhu and D. Yan, *J. Am. Chem. Soc.*, 2014, **136**, 11748–11756.
21 J. He, M. Hong, W. Xie, Z. Chen, D. Chen and S. Xie, *Journal of Controlled Release*, 2022, **351**, 301–323.
22 L. K. Ruddaraju, S. V. N. Pammi, G. S. Guntuku, V. S. Padavala and V. R. M. Kolapalli, *Asian Journal of Pharmaceutical Sciences*, 2020, **15**, 42–59.
23 M. Kim, M. Shin, Y. Zhao, M. Ghosh and Y. Son, *Small Science*, 2024, **4**, 2400280.
24 M. A. Farooq, M. Aquib, D. H. Khan, S. Ghayas, A. Ahsan, M. Ijaz, P. Banerjee, M. A. Khan, M. M. Ahmad and B. Wang, *Environ Chem Lett*, 2019, **17**, 1565–1583.
25 C. Su, Y. Liu, R. Li, W. Wu, J. P. Fawcett and J. Gu, *Advanced Drug Delivery Reviews*, 2019, **143**, 97–114.
26 G. Yang, D.-Y. Wang, Y. Liu, F. Huang, S. Tian, Y. Ren, J. Liu, Y. An, H. C. van der Mei, H. J. Busscher and L. Shi, *Bioact. Mater.*, 2022, **14**, 321–334.
27 S. G. Klochkov, M. E. Neganova, V. N. Nikolenko, K. Chen, S. G. Somasundaram, C. E. Kirkland and G. Aliev, *Seminars in Cancer Biology*, 2021, **69**, 190–199.
28 J. Majumder, O. Taratula and T. Minko, *Advanced Drug Delivery Reviews*, 2019, **144**, 57–77.
29 Y. Deng, G. Huang, S. Liu, M. Zhang, N. S. Hatzakis and Y. Jiang, *Chemical Engineering Journal*, 2024, **497**, 154452.
30 P. Das, G. Chakraborty, J. Kaur and S. K. Mandal, *Small*, 2025, **21**, 2408810.
31 M. Zhang, X. Peng, Y. Ding, X. Ke, K. Ren, Q. Xin, M. Qin, J. Xie and J. Li, *Mater. Horiz.*, 2023, **10**, 2554–2567.
32 R. Awad, A. Avital and A. Sosnik, *Acta Pharmaceutica Sinica B*, 2023, **13**, 1866–1886.
33 M. K. Shim, S. Yang, J. Park, J. S. Yoon, J. Kim, Y. Moon, N. Shim, M. Jo, Y. Choi and K. Kim, *J Nanobiotechnol*, 2022, **20**, 436.
34 S. Fu, G. Li, W. Zang, X. Zhou, K. Shi and Y. Zhai, *Acta Pharmaceutica Sinica B*, 2022, **12**, 92–106.
35 H. Mei, S. Cai, D. Huang, H. Gao, J. Cao and B. He, *Bioactive Materials*, 2022, **8**, 220–240.
36 L.-H. Liu and X.-Z. Zhang, *Progress in Materials Science*, 2022, **125**, 100919.
37 C. Liu, Q. Liu, L. Chen, M. Li, J. Yin, X. Zhu and D. Chen, *Adv Healthcare Materials*, 2020, **9**, 2000899.
38 X. Zhang, N. Li, S. Zhang, B. Sun, Q. Chen, Z. He, C. Luo and J. Sun, *Medicinal Research Reviews*, 2020, **40**, 1754–1775.
39 X. Gong, Y. Han, T. Wang, G. Song, H. Chen, H. Tang, X. Huang, K. Deng, S. Wang and Y. Wang, *Advanced Materials*, 2025, **37**, 2414357.
40 A. A. B. Patiño, V. L. Lassalle and M. F. Horst, *Journal of Molecular Structure*, 2021, **1239**, 130509.
41 C. Hu, L. Long, J. Cao, S. Zhang and Y. Wang, *Chemical Engineering Journal*, 2021, **411**, 128564.
42 S. Li, M. Pei, T. Wan, H. Yang, S. Gu, Y. Tao, X. Liu, Y. Zhou, W. Xu and P. Xiao, *Carbohydrate Polymers*, 2020, **250**, 116922.
43 X. Peng, P. Liu, B. Pang, Y. Yao, J. Wang and K. Zhang, *Carbohydrate Polymers*, 2019, **216**, 113–118.
44 S. Ali, A. Bahadur, A. Hassan, S. Ahmad, W. Shah and S. Iqbal, *Chemical Engineering Journal*, 2025, **507**, 160470.
45 L. Caselli, T. Traini, S. Micciulla, F. Sebastiani, S. Köhler, E. M. Nielsen, R. G. Diedrichsen, M. W. A. Skoda and M. Malmsten, *Adv Funct Materials*, 2024, **34**, 2405047.
46 V. A. Baulin, D. P. Linklater, S. Juodkazis and E. P. Ivanova, *ACS Nano*, 2025, **19**, 12606–12625.
47 M. Liu, F. Bu, G. Li, W. Xie, H. Xu and X. Wang, *Innov. Life*, 2024, **2**, 100076–7.
48 J. Meletiadis, S. Pournaras, E. Roilides and T. J. Walsh, *Antimicrob Agents Chemother*, 2010, **54**, 602–609.
49 C. D. Doern, *J Clin Microbiol*, 2014, **52**, 4124–4128.
50 R. Shukla, F. Lavore, S. Maity, M. G. N. Derks, C. R. Jones, B. J. A. Vermeulen, A. Melcrová, M. A. Morris, L. M. Becker, X. Wang, R. Kumar, J. Medeiros-Silva, R. A. M. Van Beekveld, A. M. J. J. Bonvin, J. H. Lorent, M. Lelli, J. S. Nowick, H. D. MacGillavry, A. J. Peoples, A. L. Spoering, L. L. Ling, D. E. Hughes, W. H. Roos, E. Breukink, K. Lewis and M. Weingarth, *Nature*, 2022, **608**, 390–396.
51 P. Zhang, X. Chen, F. Bu, C. Chen, L. Huang, Z. Xie, G. Li and X. Wang, *ACS Appl. Mater. Interfaces*, 2023, **15**, 9926–9939.
52 Y. Cai, P. Liang, Q. Tang, X. Yang, W. Si, W. Huang, Q. Zhang and X. Dong, *ACS Nano*, 2023, **17**, 11072–11072.
53 J. Guo, S. Zhang, Y. Tao, W. Zheng, H. Cheng, H. Li, Z. Wang, Y. Gou, J. Zhu, L. Li, Y. Liu, M. L. Becker and W. Tang, *J. Am. Chem. Soc.*, 2025, **147**, 14026–14027.
54 Z. Liang, Y. Chen, Z. Wang, X. Wu, C. Deng, C. Wang, W. Yang, Y. Tian, S. Zhang, C. Lu and Y. Yang, *Journal of Advanced Research*, 2022, **40**, 249–261.

The data supporting this article have been included as part of the Supplementary Information.

View Article Online
DOI: 10.1039/D5BM00879D